GOOD PRACTICE GUIDE Nº1 --- EMPIR PROJECT 19ENG05 NANOWIRES

Methodology for MEMS-fixing platform and multi-probe measurements of individual NWs

Sara Míguez[1,2], Aitor Lopeandia[1,2], Javier Rodriguez Viejo[1,2], Eleonora Cara[3], Matteo Fretto[3], Ivan De Carlo[3,4], Natascia De Leo[3], Luca Boarino[3], Václav Hortvík[5], Jan Martinek[5], Petr Klapetek[5]

[1] Departamento de Física. Facultad de Ciencias. Universidad Autónoma de Barcelona, 08193 Bellaterra, Spain.

[2] Instituto Catalán de Nanociencia y Nanotecnología (ICN2), CSIC and BIST, Campus UAB, 08193 Bellaterra, Spain.

[3] Istituto Nazionale di Ricerca Metrologica, Advanced Materials Metrology and Life Sciences Division and QR Laboratories, Strada delle Cacce 91, 10135, Torino, Italia.

[4] Politecnico di Torino, Corso Duca degli Abruzzi 24, 10141, Torino, Italia.

[5] Czech Metrology Institute, Okružní 31, 638 00 Brno, Czech Republic.

TOC

LIST OF ABBREVIATIONS

3D	Three Dimensional
AFM	Atomic Force Microscopy
ALD	Atomic Layer Deposition
EBID	Electron Beam Induced Deposition
ESEM	Environmental Scanning Electron Microscope
FEG	Field Emission Gun
FFT	Fast Fourier Transform
FIB	Focused Ion Beam
GIS	Gas Injector System
GPG	Good Practice Guide
HCP	Hexagonal Close Packed
LPCVD	Low Pressure Chemical Vapor Deposition
MACE	Metal Assisted Chemical Etching
MEMS	Micro ElectroMechanical Systems
NSL	Nano Sphere Lithography
NW	Nanowire
RIE	Reactive Ion Etching
RTA	Rapid Thermal Annealing
ROI	Region Of Interest
SEM	Scanning Electron Microscope
SiNWs	Silicon Nanowires
SThM	Scanning Thermal Microscopy

1. INTRODUCTION

This Good Practice Guide (GPG) describes two complementary methodologies enabling thermal measurements on individual nanowires. The first one uses a microfabricated MEMS structure onto which the nanowire is anchored and relies on electrical measurements. It is a dedicated technique that requires a laborious experimental protocol but provides accurate measurements of the thermal conductance of individual nanowires, while the second one, a surface-probe technique, is much faster but has lower accuracy. Reference 1 offers a comprehensive description of other methodologies to measure thermal transport of NWs.

The experimental procedures described within this GPG are related to the activities of the EMPIR 19ENG05 project Nanowires, that among other goals aims to establish specific metrology procedures to manipulate individual NWs and measure their thermal conductance with low uncertainty, below 10%, due to their interest in thermoelectric devices for energy harvesting applications. Most of the recommendations suggested in this document concerning the manipulation of the NWs and the measurement itself can be generally extrapolated to other instruments and methodologies in use for single NW thermal transport measurements.

The content of this GPG is structured as follows: It starts by briefly describing the growth of the nanowires by Metal Assisted Chemical Etching (MACE). Then, we provide details of a thermal model to achieve an optimal design of the MEMS-based suspended beams to reduce thermal losses reducing the measurement uncertainty. Next, we schematically describe the nanofabrication process of the suspended microstructure. Afterwards, this guide details the procedures of nanowires pick-up, their nanomanipulation and hanging on some MEMS suspended membranes useful for thermal analysis. The details of the setup and main instrumentation required for the electrical measurements as well as the calibration procedure are given in section 3.4, where we also explain the protocol used to perform the measurements and the main results attained. Finally, section 4 is devoted to describing the experimental setup and measurement protocol of a multiprobe Scanning Thermal Microscopy-based methodology that enables fast thermal measurement of individual nanowires supported on a substrate.

2. NANOWIRE PREPARATION: SET UP AND INSTRUMENTATION

The fabrication of porous silicon nanowires follows a combined approach of Nanosphere lithography (NSL) and MACE. NSL consists in forming a mask of ordered monolayer of polymeric spherical nanoparticles onto a substrate which is then treated with other processes as described in the following. With respect to conventional nanolithographic methods, NSL has the advantage of high throughput over square centimeter area and low-cost equipment. Similarly, MACE, an electroless anisotropic wet etching process catalyzed by the presence of a metallic mask on a semiconductor substrate, allows obtaining high aspect ratio nanostructures without the typical costing and geometrical limitations imposed by standard Reactive Ion Etching methods.

In the case of the processes concerning this GPG, prior to depositing the nanospheres, a silicon substrate was treated with oxygen plasma (40 W, 6 minutes) to increase the wettability of the surface making it hydrophilic. Plasma treatment is an alternative to a commonly used piranha solution (3:1 $H_2SO_4:H_2O_2$, 80° for 30-60 minutes) which requires longer process time and implies several risks for the operator. After the plasma treatment, the substrate is coated with a monolayer of nanospheres by spin coating which allows accelerating the evaporation of water pulling together the nanospheres in a hexagonal close packed (HCP) symmetry. This is shown schematically in Fig. 1a. The spinning speed and acceleration can be tuned to spread the nanoparticles as homogeneously as possible. SEM inspection is necessary to check the monolayer

uniformity and the number of defects. The deposition is followed by a second Ar-O$_2$-mixed plasma treatment, applied to reduce the polystyrene sphere from 100 % up to 50 % of their initial diameter while keeping their HCP position, as displayed in the scheme in Figure 1b.
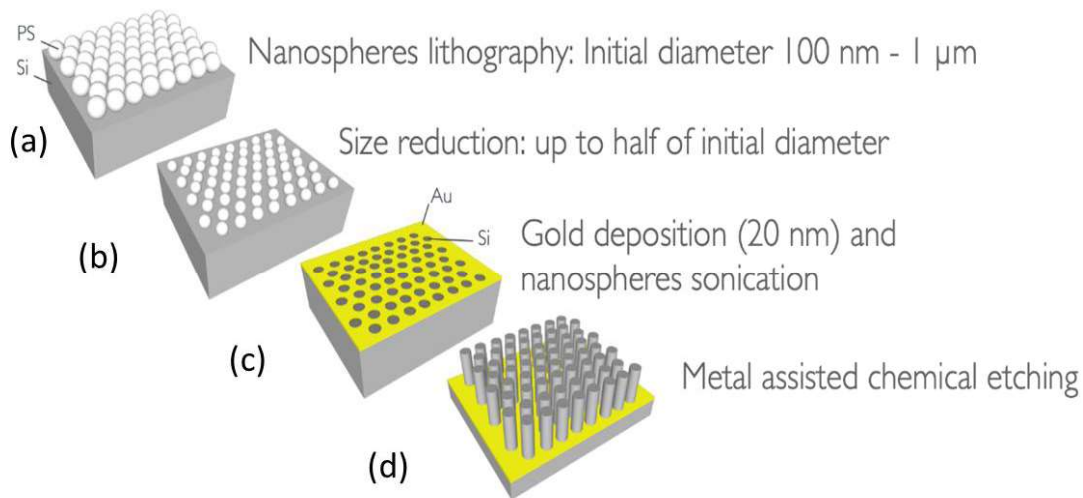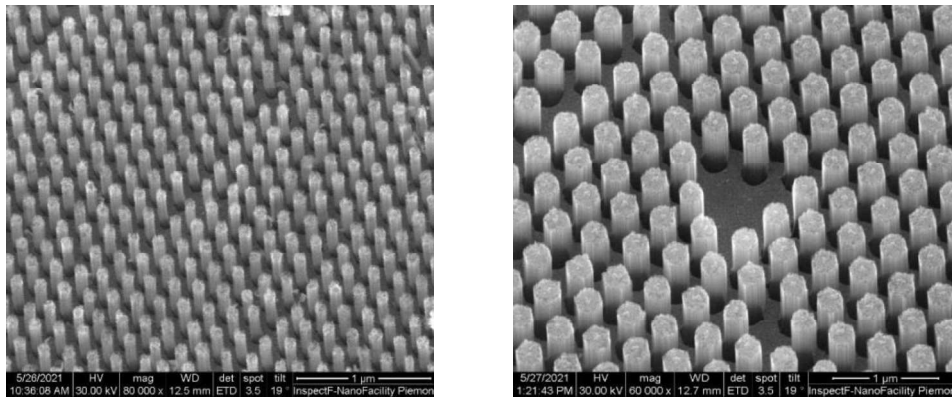

Figure 1. Processing steps diagram of porous silicon nanowires fabrication by merging NSL and MACE.

Once the desired final diameter is obtained, a 20 nm gold layer is deposited by electron-beam evaporation, then the spheres are removed by sonication, completing the NSL step and leaving a pattern of circular voids in the gold layer, as in Fig. 1c. This so-called anti-dot layer constitutes a mask for the following MACE process. The patterned substrates are immersed in an etching solution consisting of HF:H$_2$O$_2$:EtOH with ratio in volume 10:1:3. The oxidizing reactant, H$_2$O$_2$, oxidizes the underlying silicon wafer with a higher rate under the metal pattern with respect to off-metal regions. Concurrently, the etching reactant, HF, removes the silicon oxide under the metal making it possible for the metallic mask to sink into the crystalline silicon extruding an ordered array of porous silicon nanowires, as in Figure 1d, [2].

The porosity of the etched nanostructures depends both on the initial resistivity of the substrates and on the HF:H$_2$O$_2$ ratio in the etching solution, and the obtained nanowires can be crystalline (low doping < 10^{16} impurity/cm^3) or porous (high doping > 10^{16} impurity/cm^3) [3].

For light trapping and energy harvesting applications, the nanowires arrays are fabricated with a low aspect ratio (<1:10) while to perform thermal analysis for thermo-electric applications, the wires are etched with aspect ratios >1:10, typically 1:150 or 1:200, a possibility offered only by MACE as etching technique. The SEM micrographs of nanowires with different aspect ratios are reported in Fig. 2 and 3. The long wires, reported in Fig. 3, have typical length larger than 15 µm and, for this reason, they are ideal candidates to be hung on the suspended platforms across distant beams, as reported in Figures 6 and 7. The porous nanowires wires are also prone to be conformally coated with metal oxides like ZnO, TiO$_2$ and Al$_2$O$_3$ to modify and fine tune the thermal and electrical properties of the hybrid material obtained. This can be achieved by atomic layer deposition (ALD) promoting a layer-by-layer growth starting from vapor-phase chemical precursors being able to react inside the pores as well as on the external sidewalls.

EMPIR EURAMET

The EMPIR initiative is co-funded by the European Union's Horizon 2020
research and innovation programme and the EMPIR Participating States

Figure 2. Microphotos of porous silicon NWs fabricated by NSL and MACE in different operating conditions. Left: porous NWs with diameter 100 nm and height 400 nm. Right: porous NWs with diameter 350 nm and height 600 nm.
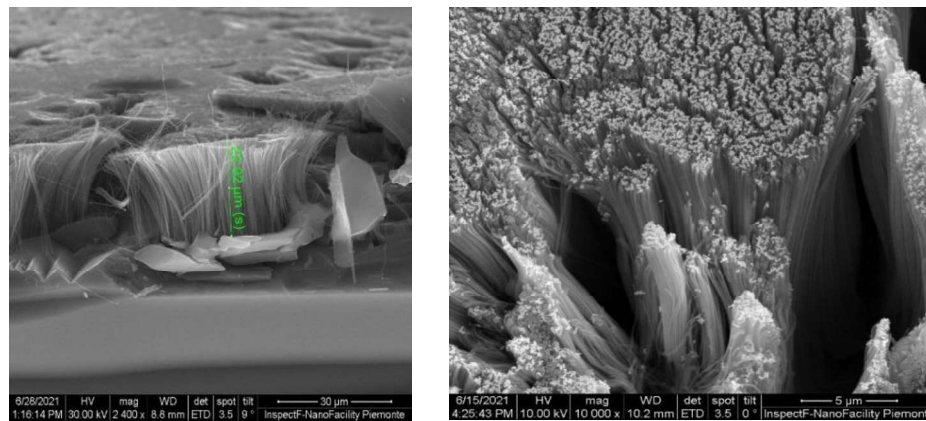

Figure 3. Microphotos of porous silicon nanowires fabricated by NSL and MACE. Left: porous nanowires with diameter 100 nm and height 22.92 μm. Right: detail of the same porous NWs with aspect ratios > 1:200.

3. ELECTRICAL-BASED METHODOLOGY USING SUSPENDED BEAMS

3.1. THERMAL MODEL

3.1.1. Design and thermal model

A necessary, but not sufficient, condition for a reliable measurement of thermal conductivity requires that the thermal conductance of the material to be measured should be higher than the thermal losses through other pathways. This is especially relevant for individual nanowires which thermal conductance can be extremely low, on the few tenths of nW/K range. Ideally, measurements should be carried out in vacuum to avoid convective and advective (which can be relevant at the nanoscale) thermal losses through air. Thermal losses by radiation can be minimized by working at temperatures not very different from the surroundings, easy to reach below 400 K, the T range explored in this project. And finally, and most important, losses through other materials in contact with the NW should be minimized. This is the reason of the suspended structures used in this study, see schematics of Fig. 4. The long-suspended low-conductivity silicon nitride beams and the thin metal lines have high thermal resistances, reducing thermal losses to the Si frame. The thermal conductance of the beams is determined by their dimensions (width, length, and thickness) since $G = \kappa \cdot \left(\frac{A}{L}\right)$, being κ the intrinsic thermal conductivity of the NW, L its length and A its section. It is important to note that minimizing the uncertainty entails appropriate values of G_b with respect to G_{NW}. This is further analyzed below.
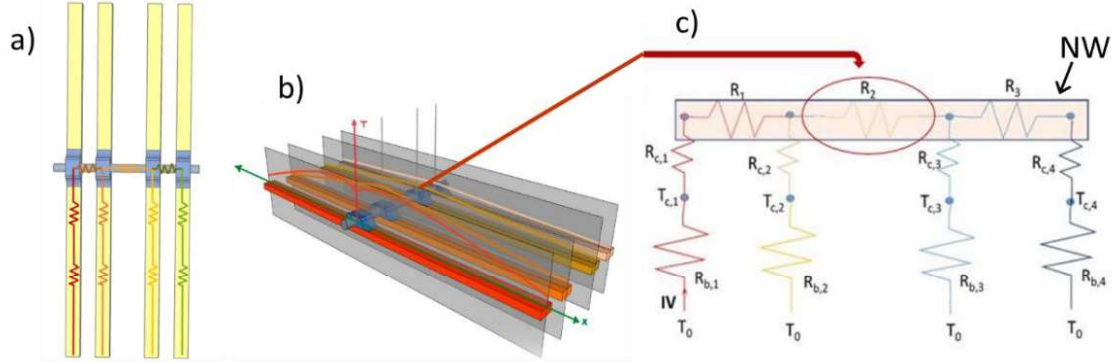
Figure 4. a) Schematic top view of the elongated beams (not to scale) and the NW placed in the middle. Blue regions are contacts. b) Temperature profiles (y-axis) in the different beams (i=1,4) while heating beam 1. c) thermal circuit indicating contact resistances ($R_{c,i}$), beam resistances ($R_{b,i}$), NW resistance (R_{NW}), thermal flows and temperature rises.

3.1.2. <u>Analytical expressions: thermal circuit analysis (simplified)</u>

The methodology used in this work follows the one developed by Shi and coworkers [4] with the use of ac current to improve signal-to-noise ratio of the measured variables. A set of equations for the thermal circuit of figure 4c can be written, as shown below. Notation is of the type $R_{j,i}$ where *i=1,2,3,4* refers to the heating beam and *j* stands for the sensing beam. For instance, $Q_{1,1}$ refers to the flow directly injected in beam *1* by Joule heating while $Q_{2,1}$ refers to the flow injected in beam *2* through the NW while heating beam *1*.

$$\Delta T_{1,i} - \Delta T_{2,i} = Q_{1,i}\left(R_1 + R_{c,1}\right) - Q_{2,i}R_{c,2}$$

$$\Delta T_{2,i} - \Delta T_{3,i} = Q_{2,i}R_{c,2} + (Q_{1,i}+Q_{2,i})R_2 - Q_{3,i}R_{c,3} \qquad \text{eq. 1}$$

$$\Delta T_{4,i} - \Delta T_{3,i} = Q_{4,i}\left(R_3 + R_{c,4}\right) - Q_{3,i}R_{c,3}$$

$$Q_{j,i} = \frac{\overline{\Delta T_{j,i}}}{R_{b,j}} \ ; \ \ \Delta T_{j,i} = 2\overline{\Delta T_{j,i}} \ ; \ \ Q_{i,i} = -\sum_{j\neq i} Q_{j,i} \qquad \text{eq. 2}$$

And the average temperature rise at the heated beam can be written as:

$$\overline{\Delta T_{i,i}} = R_{b,i}\cdot\left(P_{ac} - 2\left(\sum_{j=1}^{4}\frac{\overline{\Delta T_{j,i}}}{R_{b,j}} - \frac{\overline{\Delta T_{i,i}}}{R_{b,i}}\right)\right) \qquad \text{eq. 3}$$

where $\overline{\Delta T_{j,i}}$ stands for the average T rise in the j sensing beam, while heating beam i. From these equations (eq. 1), the temperature rises at the sensing beams and flux conservation (eq. 2) and the T increase at the heating beam (eq. 3), R_2 (the intrinsic thermal resistance of the central part of the NW between beams 2 and 3) can be calculated. This requires 16 measurements, that is heating beam i and sensing beams $j \neq i$ R_2 does not contain the thermal resistances $R_{c,2}$ and $R_{c,3}$ and therefore knowledge of the dimensions of the NW leads to an intrinsic value of the thermal conductivity.

Due to its triangular T profile the average T rise at a sensing beam is twice the maximum T at the contact point (eq. 2), while the T rise at the contact point in the heated beam is 3/2 of the average T rise.

The equations can be simplified assuming that all contact resistances are equal $\left(R_{c,i} = R_c\right)$ and that all beams have similar resistances $\left(R_{b,i} = R_b\right)$. In this case

$$G_2 = \frac{IV}{3\left(\overline{\Delta T_{1,1}} + \overline{\Delta T_{2,1}} + \overline{\Delta T_{3,1}} + \overline{\Delta T_{4,1}}\right)}\left(\frac{\overline{\Delta T_{3,1}} + \overline{\Delta T_{4,1}}}{\overline{\Delta T_{2,1}} - \overline{\Delta T_{3,1}}}\right)$$

And the uncertainty associated can be written as:

$$\delta G_2 = \frac{R_b + R_c}{Q_{1,1}R_b - \Delta T_{c2,1}} \cdot G_2^2 \cdot \sqrt[2]{\delta \Delta T_{c3,1}^2 + \left(\frac{Q_{1,1}R_b - \Delta T_{c3,1}}{Q_{1,1}R_b - \Delta T_{c2,1}}\right)\delta \Delta T_{c2,1}^2}$$

The impact of the thermal resistance of the beams can be grasped in fig. 5 where the relative uncertainty $\delta G_2/G_2$ is plotted for different values of Gb. Maintaining uncertainties below 10% as required in the EMPIR project demands adapting the resistance of the beams to the resistance of the NW, and therefore this analysis should be performed in advanced to the microfabrication process.
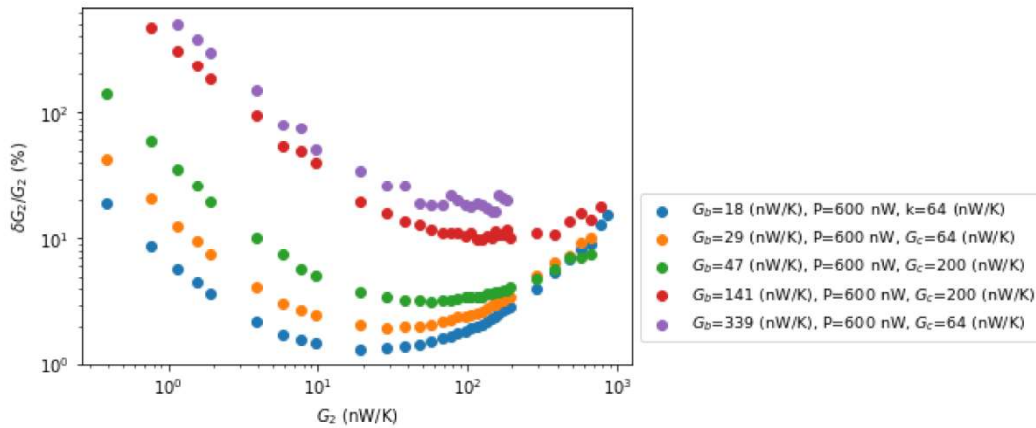
Figure 5. Relative uncertainty of the thermal conductance of section between beams 2 and 3, δG_2 vs G_2 for various values of the thermal conductance of the beams and the contact thermal conductance.

With respect to Fig. 5 note that the value of G_b for which $\delta G_2/G_2$ is smallest are those corresponding to G_b = 18 nW/K and G_b = 47 nW/K. As G_b increases, the minimum of the curves shifts to the right, but the associated uncertainties are larger. On the other hand, it is observed that for large values of G_2, the curves corresponding to G_b = 18 nW/K and G_b = 29 nW/K practically overlap, so it is concluded that both geometries in this range provide very similar uncertainties and are ideally suited to measure samples with conductance between 0.4-800 nW/K. Outside this region the uncertainty rapidly increases. G_b of the beams shown in section 3.4 are 69 nW/K. Therefore, we may expect uncertainties below 5 % for G_2 around 50 nW/K. If the value is larger may be associated to insufficient statistics or averaging of the ac signal. This is the case of the ZnO-coated porous Si NWs reported in section 3.4 that have an slightly higher overall uncertainty around 10%.

3.2. MICROFABRICATION OF SUSPENDED STRUCTURES

The measuring chips consist of multiwire suspended heater/thermometers fabricated using standard techniques. The main fabrication sequence is summarized in Fig. 6:

A) The process starts with a 4-inch silicon wafer (525m thick). The wafer will be used as mechanical support to build-in the suspended structures using different deposition, optical photolithography and etching procedures. To fulfill all requirements the original wafer should be double side polished, with a low doping to facilitate the wet and dry etchings from back or frontside (in the project we used a p-type doped with 10 Ohms·cm) and a [100] crystalline orientation to define the bulk etching openings.

B) The wafers are thermally oxidized in a furnace at 950ºC under an oxygen rich atmosphere to grow a capping layer of 100nm of silicon dioxide that ensures dielectric insulation with respect to the Si substrate. And subsequently, both sides of the wafer are coated with a low-stress silicon nitride (SiN$_x$) layer deposited by Low Pressure Chemical Vapor Deposition (LPCVD).

C) In a first lithographic process (using positive photoresist) combining e-beam evaporation and lift-off process the metallic lines and the contact pads are defined. The photolithographic mask fabricated with high resolution requirements (0.1µm resolution) considers linewidths of 1,5 µm wide with 400 µm length. The metal selection for sensor/heater was 30nm Pt with 3nm Cr as adhesion layer. Platinum is chosen for its linear dependence of resistivity on temperature and excellent chemical stability. Meanwhile, Chromium serves as an ideal adhesion layer due to its ability to withstand the subsequent hydrofluoric acid (HF) etching steps essential in the fabrication process. A rapid Thermal Annealing (RTA) is carried out to increase Pt grain size, increasing stability and the temperature coefficient of resistance, and therefore the sensitivity performance of the material as electrical thermometer.

D) A second photolithographic process with the same mask, using negative photoresist is used to protect the metallic lines and to attack the non-protected silicon nitride layer via Reactive Ion Etching (RIE) with C4HF8 and methane gas until reaching the oxide layer.

E) A 50 nm layer of SiN_x is deposited by plasma-enhanced chemical vapor deposition (PE-CVD) at low temperature to dielectrically cladding the platinum metallization. At that step, a new photolithography mask is used to selectively attack by RIE the silicon nitride deposited in between the beams and to expose the metal of the contact pads to be reached electrically with the wired bonding.

F) By plasma-enhanced chemical vapor deposition (PE-CVD) a 50 nm SiO_2 layer is deposited to protect the frontside (metal and dielectrics) in the subsequent bulk etching attacks (Dry and Wet). After spinning a mechanical protective resist in the frontside of the wafer, a layer of 400nm of Al is e-beam evaporated in the backside. With a third photolithographic mask, using a double-side alignment, windows that will define the bulk Si etching are opened in the Al layer by wet etching.

G) The beams are then suspended by etching the 525 µm of Si substrate from the backside by using a deep-RIE based on a mixture of SF_6 and C_4F_8 gases, using the Al as stopping mask. The RIE is typically stopped when the thermal oxide layer of the frontside is reached. Premature stops increase the survival ratio although some Si rests will remain. At this step, the suspended structures are still clad between the thermal oxide and the LTO capping layer. The clad membrane structure guarantees the survival of the beams during a careful dicing process performed with a minimal water flow.

H) Proceeding individually chip by chip, the cladding dielectric silicon dioxides are removed by immersion into a HF-based solution. To avoid the collapse of the beams by surface tension during drying, the chip is transferred to an Isopropyl alcohol solution, and it is let drying at low pressure and high temperatures (60°C).
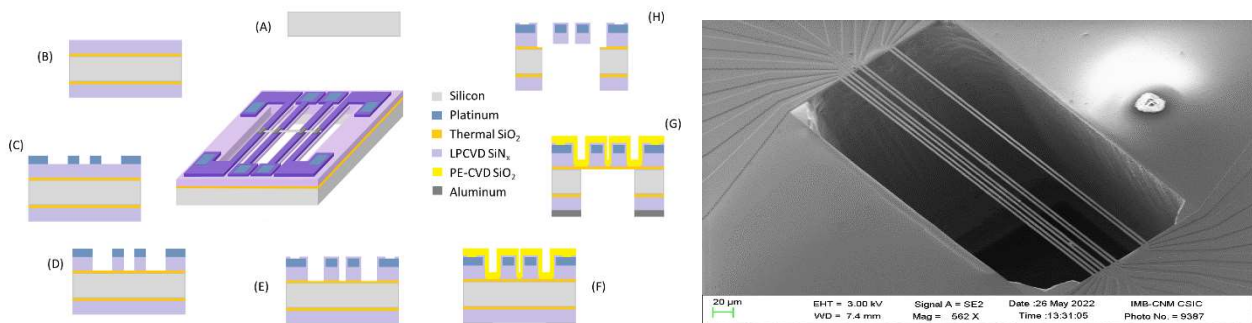
Figure 6. Microfabrication schematics and electron micrograph of a final device

To obtain a perfectly defined structure it is an essential step prior measurement since asymmetries in electrical resistances or thermal conductance of the wires would prevent accurate measurements and establish the primary uncertainty limit. Another design with two suspended platforms has also been used to measure the thermal conductance of individual porous Si NWs (Fig. 12). Its microfabrication procedure is slightly more complicated since it contains a single crystalline Si layer below the nitride platforms to improve temperature homogeneity.

3.3. NANOWIRE MANIPULATION

3.3.1. Equipment

Dual Beam ESEM Quanta 3D^{TM}

Figure 7. The Dual Beam ESEM FEG Quanta 3D™ used for the NWs manipulation. The microscope is equipped with a Focused Ion Beam (FIB) with a Ga$^+$ liquid ion source (gray cylinder inserted at 52° respect to the electron column), two Gas Injector Systems with metallorganic precursors for Pt and SiO$_x$, and four piezo-micromanipulators by Kleindiek Nanotechnik. The beam diameter is 2 nm, it can work with a column acceleration ranging from 1 to 30 kV.
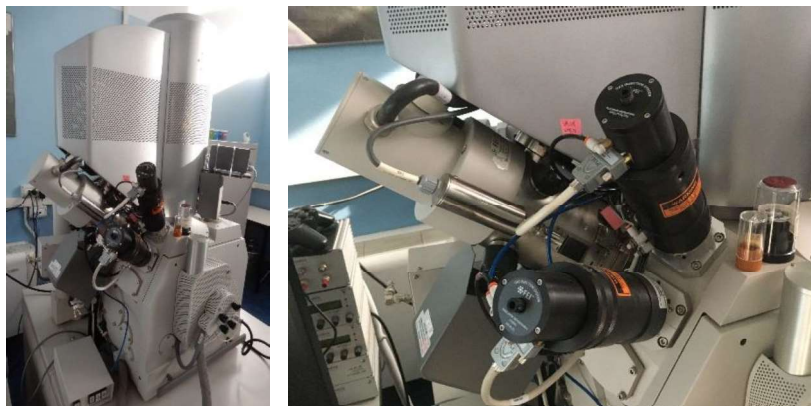

Figure 8. Details of the two GIS (black inserts) and of the FIB column (gray insert).

Nanomanipulators

The Kleindiek Nanotechnik MM3A-EM Micromanipulators are applicable to a wide range of SEM systems, the gripper arms are tungsten piezo-controlled probe tips, allowing a step size of 20 nm. Custom-shaped gripper tips are also available like RoTip and microgrippers. The tips have a typical final diameter of 100 nm and can be delivered with electrical triaxial connections [5].
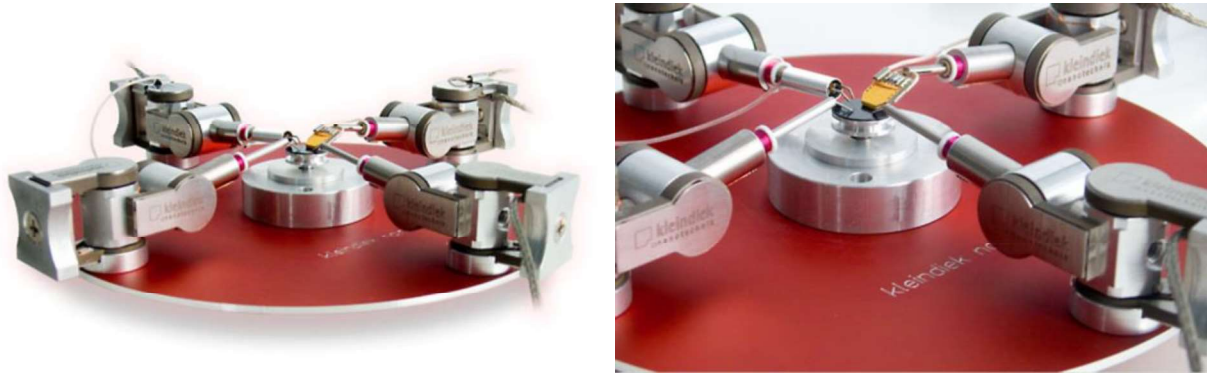
Figure 9. A typical configuration of the Kleindiek Nanotechnik MM3A-EM micromanipulators as by company flyers.
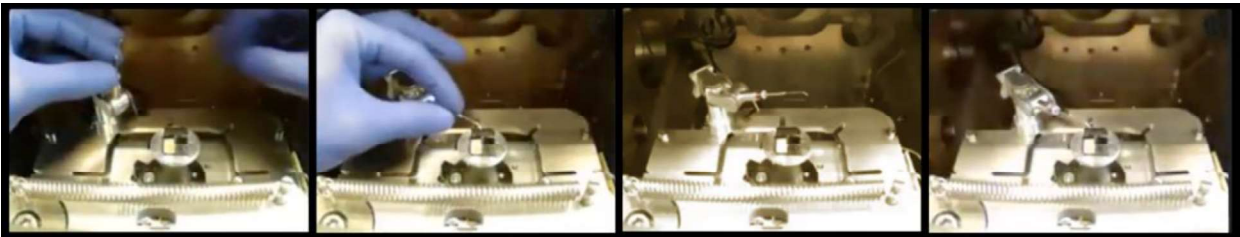
Figure 10. Mounting sequence of a Kleindiek Nanotechnik MM3A-EM micromanipulator inside the Quanta 3D™ SEM DualBeam chamber.


Figure 11. Detail of one of the four Kleindiek MM3A-EM Micromanipulators working inside the Quanta 3D™ chamber (left) and the sample holder. The controllers of the Kleindiek micromanipulators with PS2 pad controller (right). A, B and C are the three movements of the tip: A: horizontal rotation, B vertical rotation, C approaching in the tip direction.

*Kleindiek Nanotechnik MM3A-EM Micromanipulators technical specifications*:

- Three-axis manipulator
- Dimensions: 62.1 mm — 20.4 mm — 25.4 mm
- Operating range: A and B = 240°, C = 12 mm
- Speed: A and B up to 10 mm/s, C up to 2 mm/s
- Resolution: A = 10^{-7} rad (5 nm), B = 10^{-7} rad (3.5 nm), C = < 0.5 nm
- A = left / right   B = up / down   C = in / out

EMPIR EURAMET
The EMPIR initiative is co-funded by the European Union's Horizon 2020
research and innovation programme and the EMPIR Participating States

MEMS platforms for thermal measurements

Different types of MEMS platforms for the measurements of thermal properties of silicon nanowires have been designed and developed at UAB, Universitat Autònoma de Barcelona (Spain). In the framework of the EMPIR project 19ENG05 Nanowires, we have used mainly two types of platforms: a four-beam structure (Fig. 13) and a double Pt heater/thermometer suspended on two SiNx platforms (Fig. 12) [6,7].
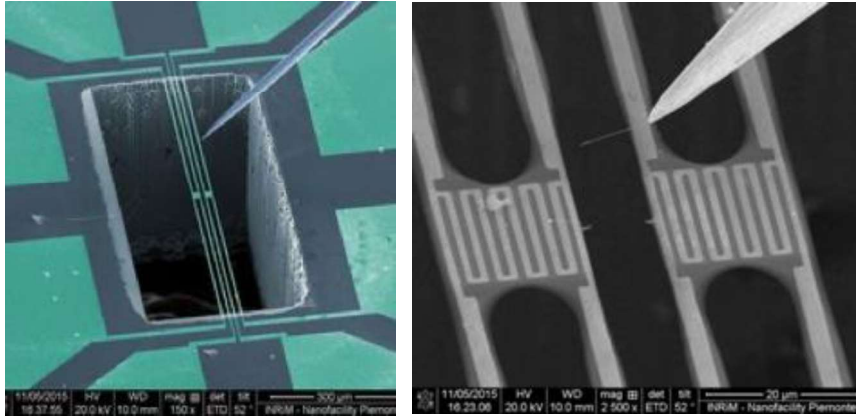
Figure 12. MEMS platform Type 1 by UAB [6,7]: Si_3N_4 tethered stripes (couples of 4 μm wide and a few hundreds of micrometers long) are suspended onto a hole through the entire silicon wafer realized by a Deep Reactive Ion Etching (left). In the center of the suspended stripes, two squared membranes host two Pt meanders connected to the external bigger pads for bonding (the detail on the right). These two meanders can both act as a heater and thermometer. The nanowires must be hung and bonded in the middle of the central gap between the two meanders.
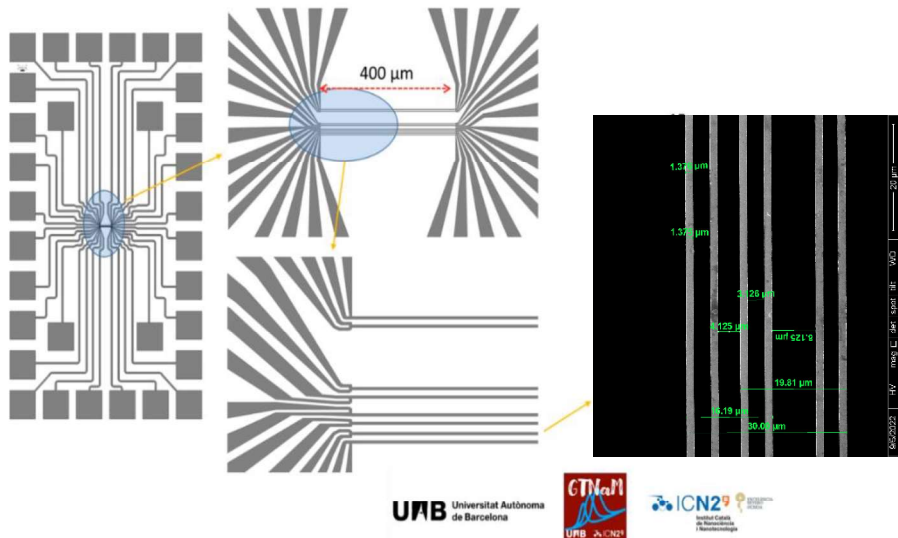

Figure 13. The MEMS structure with the suspended beams is more reliable for thermal transport measurements. It consists of a central region (highlighted in the insets) with 8 suspended beams at different reciprocal distances to allow mounting nano-objects of different lengths across four (or more) of them to perform thermal transport measurements. In the rightmost inset, widths and distances between beams are reported. The nanowire should be positioned perpendicular to the beams. All around the central suspended structure, large contact pads are present. Another, larger view, SEM micrograph is shown in Fig. 6.

### 3.3.2. Nanowires pick-up and bonding

Before the nanowires pick up procedure, the sample should be prepared to detach a single nanowire and place it in a horizontal position. Two different approaches were studied: 1) the nanowires are scratched with

cleanroom paper on a silicon wafer covered by a thin layer of silicon oxide; 2) the nanowires are scratched and left on the matrix of other silicon nanowires realized by MACE. The first approach guarantees to have nanowires in a perfect planar position but could result in a difficult contact with the tip of the micromanipulator caused by an electrical field moving the nanowires during the process. The second approach requires a longer phase to select the nanowire in the proper position but guarantees an easier phase of tip contact. Usually, the second method is preferred. The pick-up process can be performed at any sample holder tilt, anyway 20-30° tilt is recommended during the approach of the nanomanipulator tip approach to better understand the point of contact on the sample surface. The sample holder should be placed in eccentric position when the GIS needle is inserted. The nanowires array sample with the scratched nanowires is inserted into the microscope vacuum chamber together with the nanomanipulator (Fig. 14).
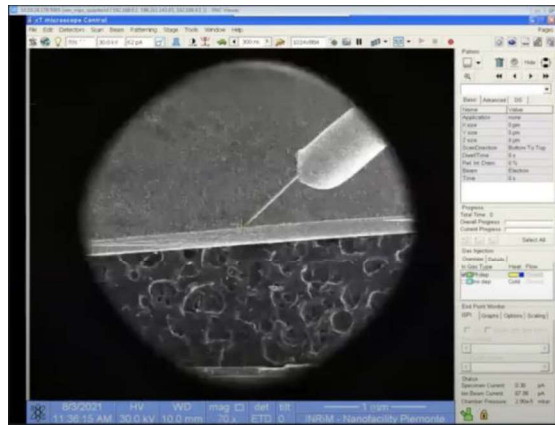

Figure 14. A low magnification SEM image of the array sample and the detail of a nanomanipulator and its tip inside the microscope vacuum chamber.

The first phase consists in the imaging of the nanowires to look for a suitable nanowire to be manipulated. Once a nanowire is for its suitable position and length, it is approached with the nanomanipulator (Fig. 15).
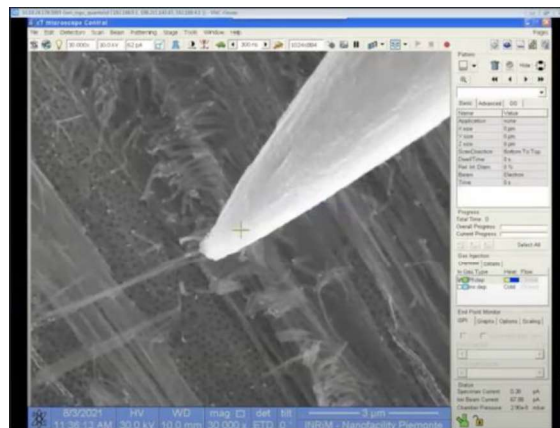

Figure 15. A nanowire was identified as suitable for the nanomanipulation and location on the platform for thermal measurements, due to its suitable position and length. In this SEM image, it is possible to observe the nanomanipulator tip approaching the nanowire.

The tip of the nanomanipulator is soldered to the nanowire by a platinum patch obtained by exploiting a gas injection system (GIS) previously inserted in the chamber. GIS releases a Pt-based metalorganic precursor in vapor phase, $(CH_3)_3Pt(CpCH_3)$, and, through the interaction between the Pt vapor and the electron beam rastering that area, metallic Pt is deposited in a selected area. This process is the so-called electron-beam-induced deposition (EBID), [8,9]. The sequence of the nanomanipulator approach and platinum deposition is reported in Fig. 16.
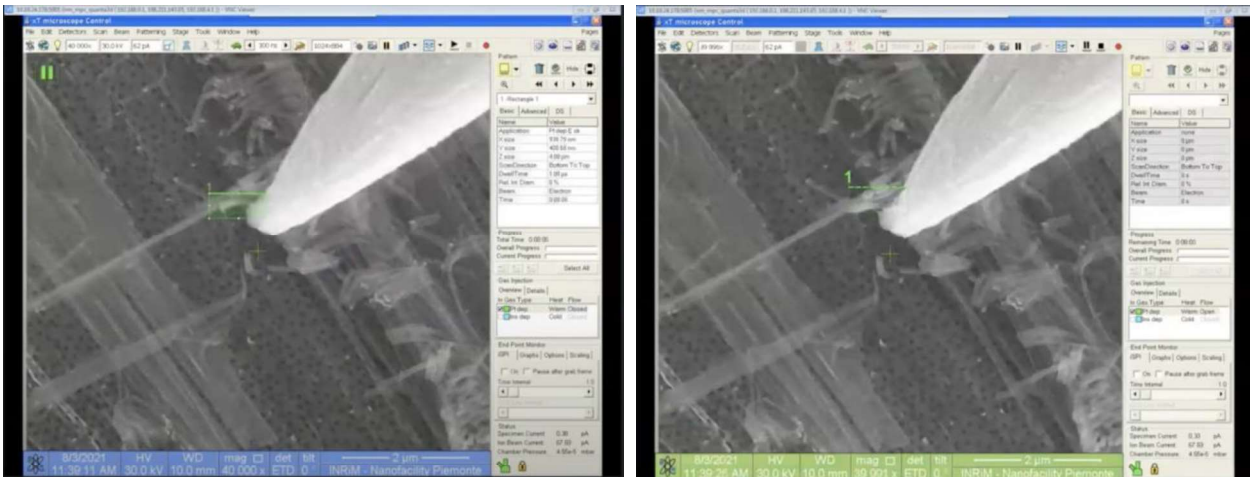
Figure 16. A sequence of SEM images showing the soldering of the nanowire to the nanomanipulator tip. Left: The SEM image shows the large GIS needle, next to the thin nanomanipulator tip in contact with the nanowire. Right: The SEM image shows a bright green rectangle being designed on top of the nanomanipulator tip and of the nanowire, this is the area where the EBID deposition will occur. The green bar at the bottom of the SEM image indicates that the platinum deposition is on-going in the green rectangular area.

After the nanowire pick-up phase is completed, the nanowire is attached to the nanomanipulator tip through a Pt patch as visible in Fig. 17. The nanowires can be moved around the microscope vacuum chamber through the nanomanipulator motors, and it can be brought in proximity to the platform where it should be deposited. The MEMS platform chip can be loaded in the microscope vacuum chamber concurrently to the nanowire's matrix substrate used during the pick-up phase. In some cases, when the MEMS platform chip is too large, one would have to unload the pick-up matrix and load the MEMS platform chip, however, this additional step introduces some concerns regarding the hand operations in proximity to the nanomanipulator and the suspended nanowire, so extra attention should be paid in this occurrence.
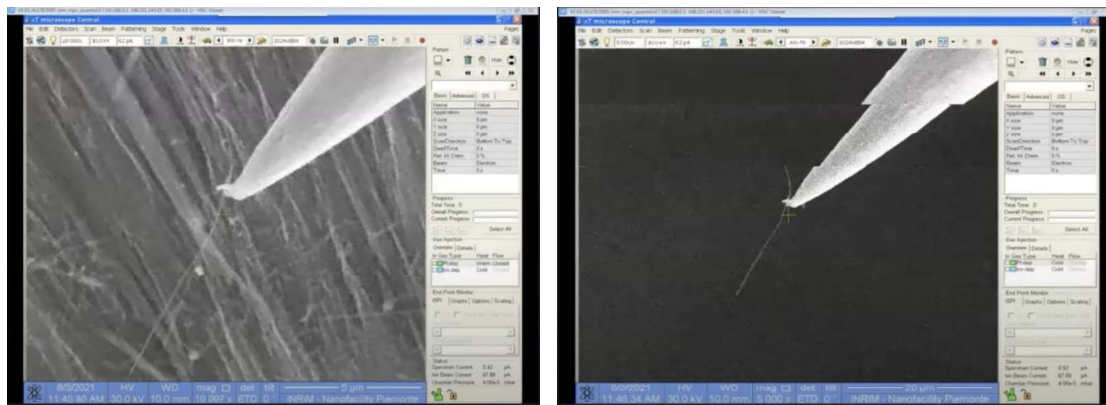

Figure 17. SEM images showing a nanowire attached to the nanomanipulator tip through a Pt patch and suspended in empty space inside the microscope vacuum chamber.

The microscope motorized stage can be moved so to position the MEMS platform chip underneath the nanomanipulator tip. Once in the correct position is found, the nanomanipulator can be brought to approach the platform or the suspended beams by progressively lowering its z-height and correct its xy position.

Once the nanowire is near the suspended beam structures it is soldered to the beams with small patched of platinum deposited via electron-beam-induced deposition (EBID) starting from a metalorganic precursor of Pt injected in the microscope chamber through a gas injection system (GIS) needle. The nanowire is attached to the beam at the end opposite to the nanomanipulator. Subsequently it is lowered with the

nanomanipulator to reach all other beams. The result is shown in the images in Fig. 18. The nanowire is inspected at high tilt angle to ensure the contact is established, if necessary, the Pt patches can then be strengthened to ensure good thermal contact and stability for the delivery of the device.
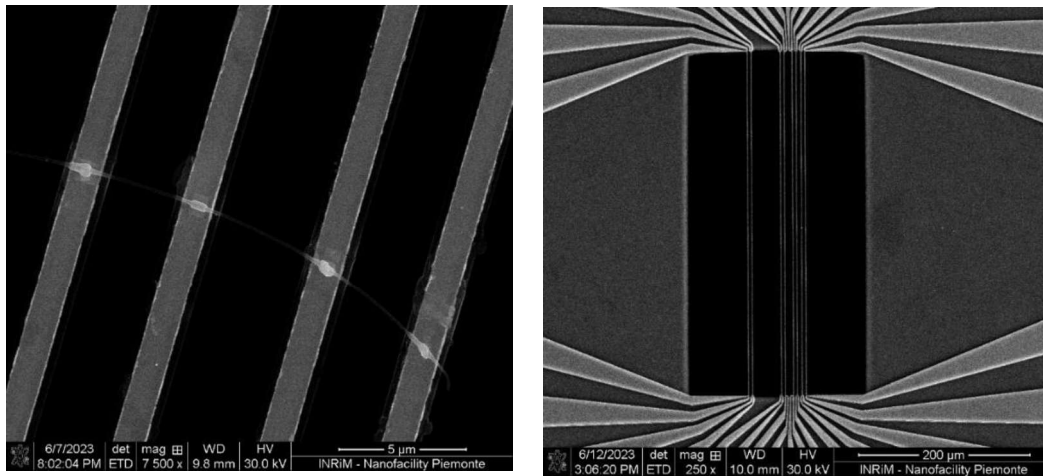
Figure 18. The SEM image on the left shows the nanowire soldered to the four suspended beams through small patches of Pt precisely deposited by GIS and EBID. The SEM image on the right shows the entire area of the suspended beams at low magnification. The nanowire is placed at approximately equal distance from both edges.

3.4 ELECTRICAL-BASED MEASUREMENTS IN SUSPENDED STRUCTURES

3.4.1. Set up and instrumentation for thermal measurements

Here we describe the equipment used within the EMPIR project to measure the thermal conductance of individual porous Si NWs coated with ALD-ZnO.

A) The electronic chain

The principle of thermal conductance measurement relies on precise measurement of changes in resistance of metallic beams, and consequently, the mean temperature of the beams, while applying controlled power to heat other beams (as previously explained in the measurement protocol). In a specific scenario where a nanowire sample with low thermal conductance (few nW/K) is loaded into the measuring structure using nanomanipulators and FIB for bonding, when one of the beams is heated to a few Kelvin, the remaining beams experience a temperature rise ranging from a few hundred millikelvin (the closer beams) to a few tens of millikelvin (the most distant beams).

To ensure accurate measurements in such cases, it is crucial to maintain the temperature stability of the measuring chip (the reference temperature) as constant as possible, thereby minimizing any derived uncertainty. This stability is essential for obtaining reliable thermal conductance data from the experiment.

For this reason, the measuring chips are loaded into a closed-cycle Helium cryostat from Advanced Research Systems (ARS). Equipped with radiation shields, the cryostat allows for operation in a broad temperature range, spanning from 4 to 350K, all under high vacuum conditions. To optimize sensitivity in measuring the holder's temperature, particularly around room temperature, the system has been equipped with a cryogenic Pt100 sensor. At high temperatures the Pt100 sensor exhibits superior temperature sensitivity compared to the preinstalled Si diode thermometers, enabling more accurate temperature measurements. To achieve improved temperature stability, a custom-built temperature PID controller based on Labview, in conjunction with high-resolution power source (Agilent E3641A DC) and meters (Keithley 2000), is utilized. This combination ensures temperature stabilities of around 1 millikelvin at room temperature, providing precise control over the experimental conditions. Custom-built high diffusive sockets were meticulously designed and fabricated using commercial aluminium PCBs to precisely load chip samples into the cryostat finger. The

chip samples can be conveniently attached to the sockets using silver paste and securely wire bonded, ensuring stable electrical connections. To establish reliable connections to the cryostat feedthroughs, pico-clasp connectors are employed. Additionally, an external multiconnection box is used to efficiently manage and route multiple wires, streamlining the experimental setup and facilitating smooth data acquisition during the 16 measurements. This comprehensive approach guarantees the integrity and accuracy of the experimental process, allowing for precise thermal conductance measurements in the cryostat.
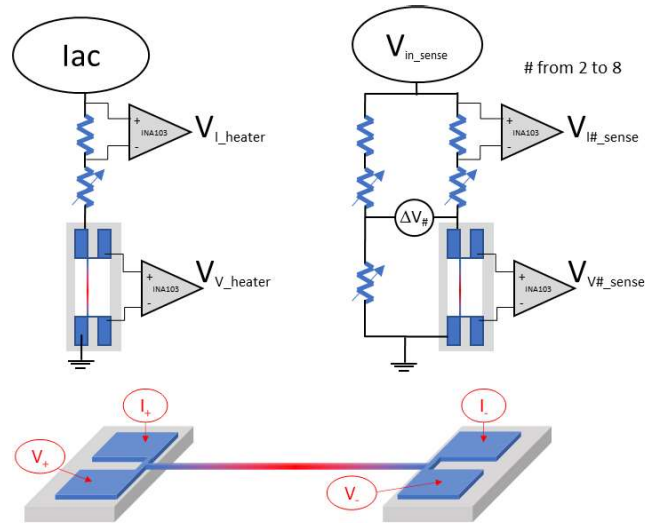
The thermal measurements are taken in selected pairs of beams: heating in one and measuring in a second. The measurement approach considers the use of AC signatures to taken profit of lock-in strategies to enhance the measurements sensitivity. The measurements are taken feeding with oscillating currents at frequencies over 600 Hz, since characteristic thermal response of the microbeams is around 10Hz, and therefore the temperature oscillation of the beams in negligible and the measurement resembles the DC approach. These uncoupling of thermal and electrical response of the beams is crucial for the enhanced sensitivity.
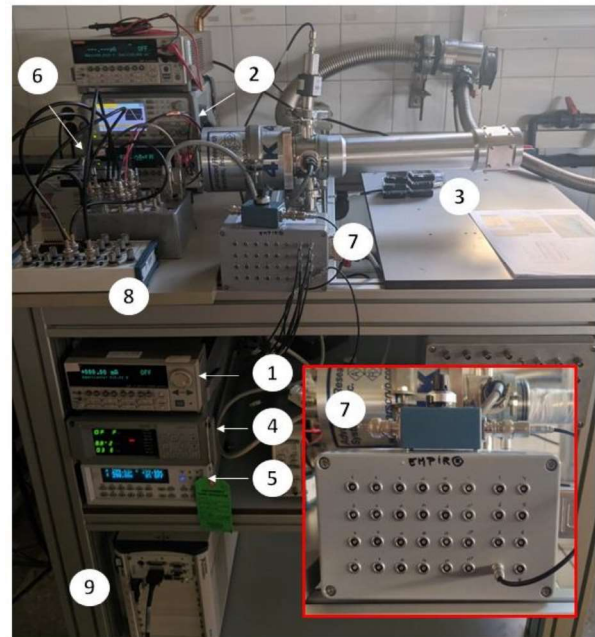
Figure 19. Experimental setup showing (1) Keythley 6221 multimeter to feed heated beam, (2) Agilent 33500B to feed sensors, (3) Cryostat, (4) Pressure monitor, (5) LakeShore commercial PID controller, (6) Keythley 2000 multimeter to measure Pt100 values and determine temperature, (7) Multiconnection box, (8) NI Card connection interface and (9) NI-PXI-8187 Rack equiped witha Ni-PXI-6123 data acquisition card.

Fig. 20 (A) shows a schematic of the electronic chain used in the measurement of each pair of beams. On the left, the heated beam is feed with an Keythley 6221 AC current source, amplitudes are typically ranging from 5 to 50μA, with frequencies around 650 Hz. The measurement chain considers a branch with a load reference resistor (50KΩ) that is used to effectively measure the current passing through the beam by measuring the voltage drop in it (called Vi_Heater). In four wire configuration the voltage drops in the beam resistor (Vv_Heater) is measured with the aid of an instrumentation amplifier the decouples the measurement chain from the samples. The selected instrumentation amplifier is the INA103 that exhibit an extremely input voltage noise (~1nV/√Hz) and a quite good output noise (~65nV/√Hz) that working with amplifications factors over 100 permits to work in (or close to) the Johnson-Nyquist noise limit.

The measurement chain for the sensed beam is based on a Wheatstone bridge configuration. Like in the heating branch a load reference resistor (50KΩ) is used to measure the current flowing through it. In that se the bridge is fed by an Agilent 33500B dual true-form wave generator. The voltage drop in the sensed beam can be directly measured in four wire configurations using a twin amplification chain to the one presented

for the heating branch. The bridge configuration permit also to measure in differential configuration (x1000) the relative variation of the beam resistance to one reference resistor (or to an extra beam isolated from those connected with the nanowire). Differential measurements are especially suited if the temperature stability of the static holder is not stable enough. To feed the sensed beams the voltage amplitude of the generator is fixed to achieve currents around 5 µA, that produce almost negligible self-heating, and the frequency is fixed closed to the heating one, typically 20Hz over it. Although electronic cross-talking between beams is very small, in some devices capacitive coupling can be detected when

Figure 20. Schematics of the measurement setup.

measuring the differential signature and the improvement respect to non-differential measurements is moderated if sample temperature stability is good.

For these experiments, a Labview program based on Fast Fourier Transform Analysis (FFT) has been designed substituting analogic Lock-in amplifiers. Using a simultaneous data acquisition card NI-PXI-6123 raw data signals are acquired as a function of time, in differential mode at acquisition rates of 500 KSamples/s per channel. Acquiring around half a million samples, around 1s integration time, the total sample package is cut to be an integer multiple of the base frequency (both for heating an sensing channels) to prevent spurious high frequency component in the FFT. The amplitude of the first harmonics of the measuring signature is routinely acquired with signal to noise ratios better than 10^5. With this resolution resolving the voltages in 1s, Ohm's Law permits to infer the beam resistance, and even with current values of few µA, with resolutions better than 10mk, close to the Johnson limit for the sensor. Since the reference temperature in a good experiment is maintained within few mK, statistical measurements permit to improve close to 1 order of magnitude this resolution limit approaching the mK limit.

3.4.2. Calibration

Although not mandatory, before placement of the NWs onto the suspended beams, it is convenient to perform a precise T calibration to determine the temperature coefficient of resistance of the metallic lines and the thermal conductance of the long nitride beams. Temperature calibration should be carried out in the appropriate T range ensuring a good base temperature stability. In this project measurements were carried out inside a closed cycle He cryostat with a temperature variation below 2 mK at the setpoint temperature, as shown in Fig. 23 right panel.

In steady state a temperature increase in the Pt lines will induce a resistance increment given by $R = R_0(1 + \alpha\overline{\Delta T}) = R_0 + R_0 \frac{R_0\alpha}{G_b^{app}}I^2$, where $\overline{\Delta T}$ is the average T rise in the heated beam. The protocol is the following. We measure the change of R as a function of the input current through the Pt line and build curves of R vs I^2 at each base temperature. The R_0 at each T is obtained from extrapolation at $I=0$. Then, a plot of R_0 vs T (Fig. 21 left) gives a straight line with a slope $R_0 \cdot \alpha$ from which alpha is obtained. Then, from the knowledge of $R_0(T)$ and alpha the apparent thermal conductance of the beam while heated can be deduced, G_b^{app}. It can be shown than when the measurement is carried out in the heated line the T profile is parabolic and therefore a correction should be applied which gives $G_b = G_b^{app}/3$.
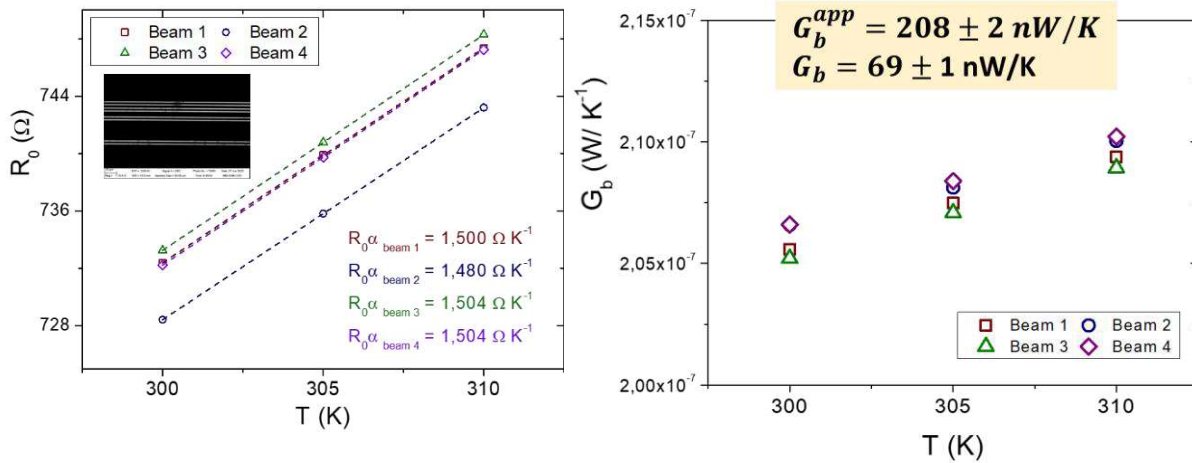
Figure 21. (Left) Resistance of the heated line *i* and (right) value of the apparent thermal conductance of the beam as a function of the base temperature.

In parallel we will also determine the impact that heating line *i* has on the temperature rise of the other beams $j \neq i$ by near-field radiation.
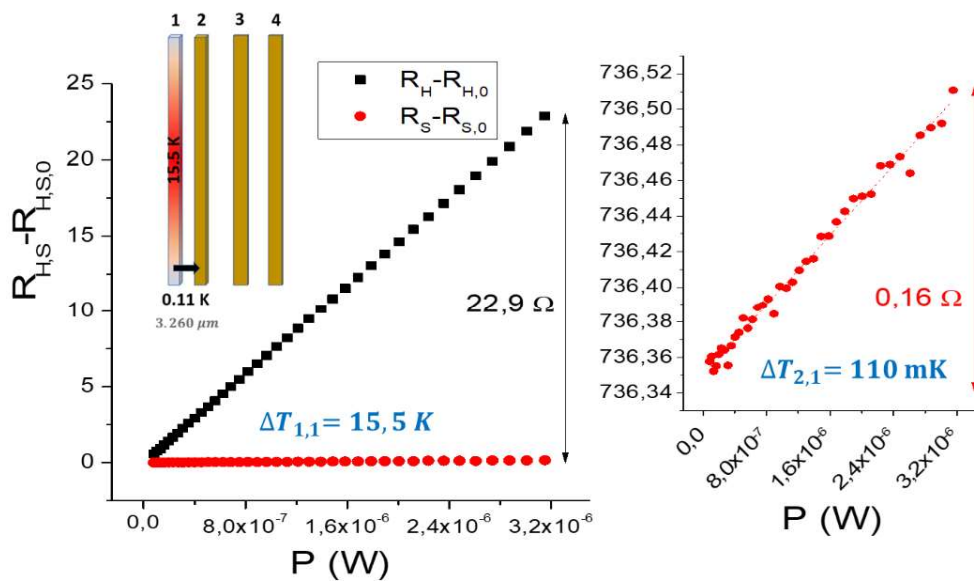
Figure 22. Resistance variation versus power for beam 1 (heater) and beam 2 (sensor). The T rise at the highest injected power to beam 1 is marked in blue.

Figure 22 shows an example of the impact of heating one beam on the temperature rise of the other beams by radiation effects. In this case, heating beam 1 to 15,5 K above the frame temperature rises beam 2 by 110 mK. This corresponds to a conductance by this mechanism of near-field radiation of G_{link}=1,34 nW/K. The importance of this value depends on the conductance of the NW, but for low conductance NWs the T rise due to this mechanism should be subtracted to improve accuracy. Table I lists the G_{link} values for different beams.

Heater	Sensor	G_{link} (nW/K)
1	2	1,34
2	1	1,20
2	3	0,58
3	2	0,59
3	4	1,21
4	3	1,11

Table I. Thermal conductance due to near-field radiation on neighbor beams to the heated beam

3.4.3. Nanowire thermal conductance: Measurement protocol & results

Once the NW is located on top of the beams, as explained in section 3.3, we carry out a series of measurements where the four beams (i = 1,2,3,4) are heated and beam i and $j \neq i$ are measured.
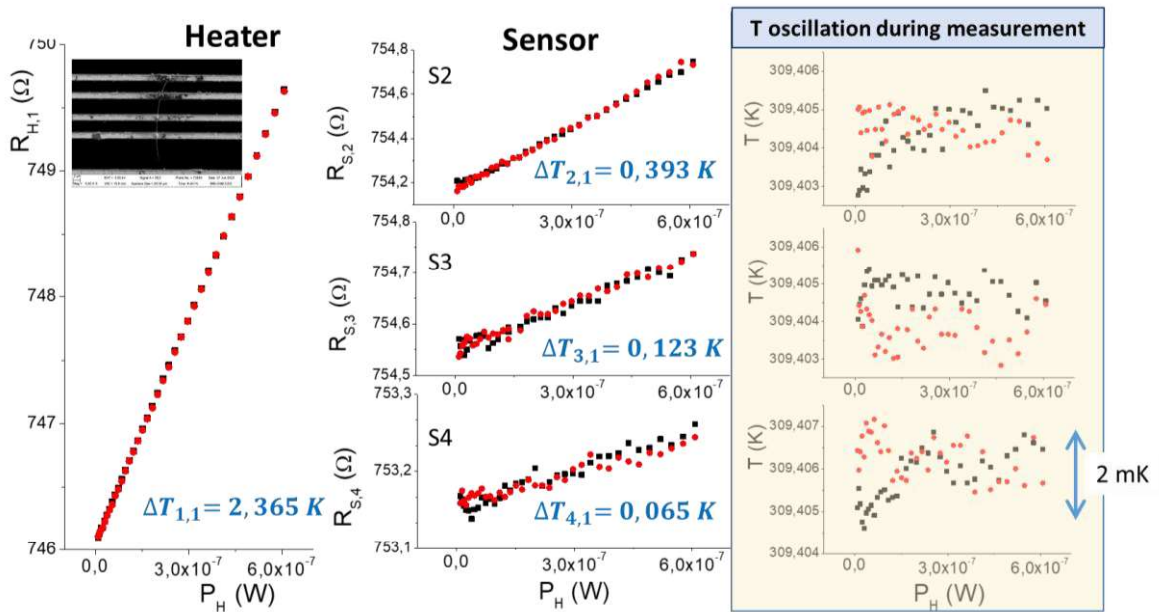
Figure 23. Example of the measurement when beam 1 is heated at several input powers (P_H) and the temperature (resistance) increase in beams 2,3,4 is sensed for each input P_H. The right panel (yellow colored) shows the base temperature of the sample holder during the measurement with oscillations below 2 mK.

By heating the four beams we can extract the values shown in Table II.

H (i)	S (j)	$\overline{\Delta T_{i,i}}$ (K)	$\overline{\Delta T_{j,i}}$ (K)
1	1	2,365	
1	2		0,393

|			
1	3		0,123
1	4		0,065
2	2	2,030	
2	1		0,373
2	3		0,374
2	4		0,179
3	3	1,923	
3	1		0,130
3	2		0,337
3	4		0,560
4	4	2,145	
4	1		0,052
4	2		0,177
4	3		0,569

Table II. Average temperature rise for heated and sensor lines evaluated at the maximum input power, P=6,1x10^{-7} W.

The conductance of the central part of the NW between beams 2 and 3 (G_2) can be extracted under different circumstances. If we assume $R_{b,i} = R_b \, \forall \, i$ and $R_C = 0$, we can use data obtained using beam 1 as heater to evaluate G_2 as

$$G_2 = (R_2)^{-1} = \frac{P_{ac}}{3\left(\overline{\Delta T_{1,1}} + \overline{\Delta T_{2,1}} + \overline{\Delta T_{3,1}} + \overline{\Delta T_{4,1}}\right)} \left(\frac{\overline{\Delta \mathrm{T}_{3,1}} + \overline{\Delta T_{4,1}}}{\overline{\Delta T_{2,1}} - \overline{\Delta T_{3,1}}}\right) = 47,8 \text{ nW/K}$$

Similar values can be derived when heating beams 2,3 and 4. See Table II, from which an average thermal conductance and the associated uncertainty can be derived,

$$G_2 = 43,4 \pm 4 \text{ nW/K}$$

Considering than the average diameter of the NW between beam 2 and 3 is 250 nm and the length 5,4 µm (Fig. 24) the thermal conductivity can be extracted, $\kappa = \frac{G_2 \cdot L}{A} \approx 6,1 \pm 0,6 \; W/mK$. This value is slightly larger than the one previously obtained on uncoated porous Si NWs grown with the same methodology [6], i.e. $\kappa \sim 2 \; W/mK$ for a 250 nm NWs. The difference may be attributed to the ultrathin ZnO layer grown by ALD. We note however that the electrical conductivity may increase by orders of magnitude due to the ZnO overlayer and therefore these NWs may be of interest for thermoelectric applications. The uncertainty of the thermal conductivity is shared between the measurement of G_2 and the uncertainty associated to the dimensions of the NW, given the fact that the diameter is slightly different at both ends
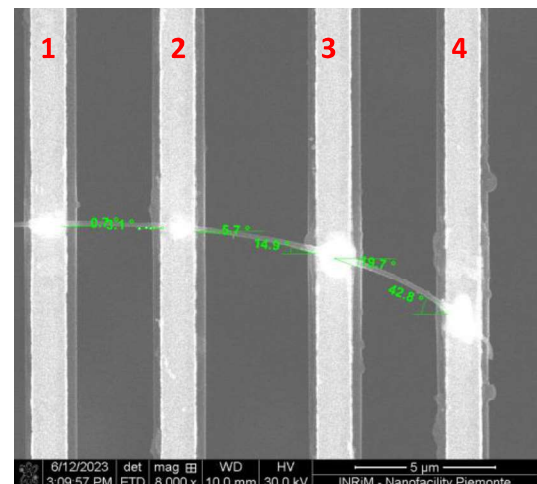
Figure 24. Magnification of the NW located between beams 1 to 4.

(beams 2 and 3) and that the outer diameter is difficult to estimate with high precision due to the intrinsic porosity of the nanowire. More statistics and averaging in the measurement of G_2 and resolution of the thermal circuit through the complete set of equations may reduce the uncertainty well below 10%.

If we assume $R_{b,i} = R_b \ \forall \ i$ and $R_{c,i} = R_c \neq 0$, we can use data obtained using beam 1 and beam 2 as heaters to evaluate G_2 as

$$G_2 = (R_2)^{-1} = \frac{4 \cdot P_{ac}}{9} \frac{\left(\overline{\Delta T_{2,1}} - \overline{\Delta T_{3,1}}\right)\left(\overline{\Delta T_{3,2}} + \overline{\Delta T_{4,2}}\right) + \left(\overline{\Delta T_{4,1}} + \overline{\Delta T_{3,1}}\right)\left(\overline{\Delta T_{1,2}} + \overline{2\Delta T_{3,2}} + \overline{\Delta T_{4,2}}\right)}{\left(\overline{\Delta T_{2,1}} - \overline{\Delta T_{3,1}}\right)\left(\overline{\Delta T_{1,1}} + \overline{\Delta T_{2,1}} + \overline{\Delta T_{3,1}} + \overline{\Delta T_{4,1}}\right)^2}$$

$$G_2 = 45{,}5 \ nW/K$$

This value lies within the uncertainty obtained previously, which already indicates the contact thermal resistance may not play a relevant role due to the low thermal conductance of these NWs.

Other approaches that consider all $R_{c,i}$ and $R_{c,i}$ may be different can be used to determine G_2.

4. MULTIPROBE STHM MEASUREMENTS

Goal of the two-probe Scanning Thermal Microscopy experiment was to use commercially available Scanning Probe Microscope and modified commercially available thermal probes to determine thermal conductivity of an individual nanowire, minimizing the impact of heat flux towards the substrate. The two-probe geometry is shown, both schematically and as a microscope camera view, in Fig. 25. In contrast to the MEMS platform this represents a relatively simple and fast way how to use multi-probe techniques for nanowires characterization, as it needs almost no sample preparation - the studied nanowires were only placed on a flat substrate with low thermal conductivity.
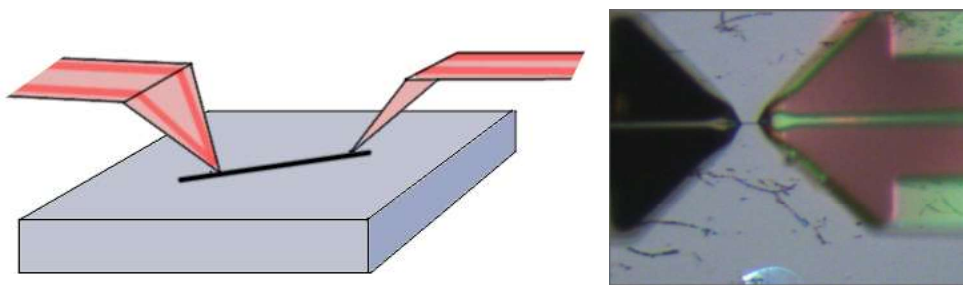
Figure 25. Schematics of the two-probe experiment and optical view on the two probes in the Dimension Icon microscope.

4.1. EXPERIMENTAL SETUP

To introduce two Scanning Thermal Microscopy probes inside a commercial microscope, Dimension Icon from Bruker, we had to make some changes on the probes, as shown in Fig. 26. First, the commercially available VITA-DM-GLA1 probe printed circuit board support was cut to create space for the second probe in the microscope. The probe was inserted to the Icon scanner using only two of the four pins of the probe attachment setup, which was proven to be enough for stable operation. Second, another probe was cut completely from the printed circuit board support and glued and bonded onto a simple holder that was attached to a combination of manual and piezoelectric positioners, to be able to place it close to the first probe. For this, the optical camera of the Icon microscope was used. Two independent custom built SThM

electronics were constructed, based on a Wheatstone bridge with one adjustable branch excitated with regulated constant voltage source driven by precision voltage reference. The signal was amplified using AD8429 precision instrumentation amplifier. The stability has been tested using 400 Ohm resistor instead of the SThM probe, that reveals that the residual readout related uncertainties come from the probe but not the electronics. The electronics was designed to be galvanically separated, either using transformer or batteries. Two units were used to control the probes and to read out the bridge values in most of the experiments, however, the measurement was possible also using commercial VITA electronics provided by Bruker, which provides basically the same results, only the circuitry details are out of our control.

Having two probes in the system and being capable of move them individually allows performing many different types of experiments, however from practical purposes we used only one combination:

- the probe on the holder, called here the fixed probe, was brought above a nanowire using an optical camera and then into contact with the nanowire using a piezoelectric actuator. To control the position in the z direction the thermal signal was used. The probe was either heated (acting as heat source) or kept at minimum current necessary to read the temperature (acting as heat sink).
- the probe on the Icon scanner, called here the moving probe, was used to perform Force Volume measurements.

Use of Force Volume regime for all the measurements was necessary to prevent movement of the nanowires across the surface. In this regime the probe performs a Force-Distance curve at every pixel. Force-distance curves parameters were chosen to maximize the displacement, i.e. typically the curve length was 6-8 micrometers. Even if the typical "far from sample" reference in SThM is suggested to be much larger, in hundreds of micrometers, having an out-of-contact reference value in every pixel can be used to normalize the data against drifts. The curve acquisition rate was typically 2-3 Hz, and this value was determined from the approach-retract thermal signal differences, to prevent probe thermal inertia to affect the result (reported and measured reaction times of this types of probes are between hundreds of microseconds and milliseconds). Hold time at maximum force was 100 ms. Moreover, using Force Volume regime allowed us to use the moving probe to scan across the fixed probe, adding traceability to the probe-probe distance, as shown in Fig. 27.
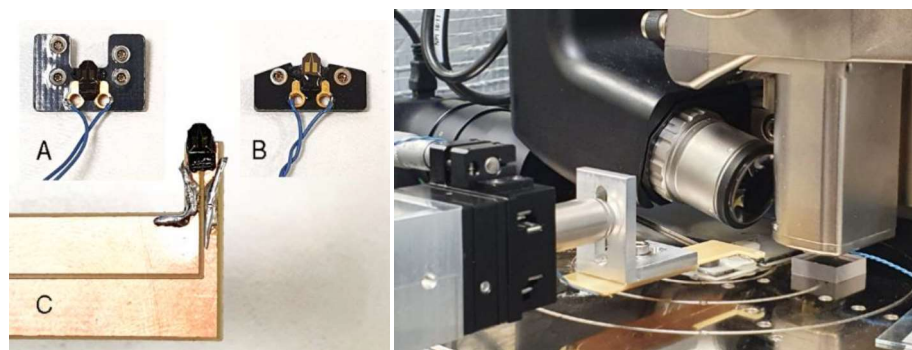

Figure 26. Left - probe preparation A: original VITA-DM_GLA1 probe, B: probe cut to gain extra space, C: probe on the holder, right - the overall picture of the fixed probe inserted in Dimension Icon microscope.
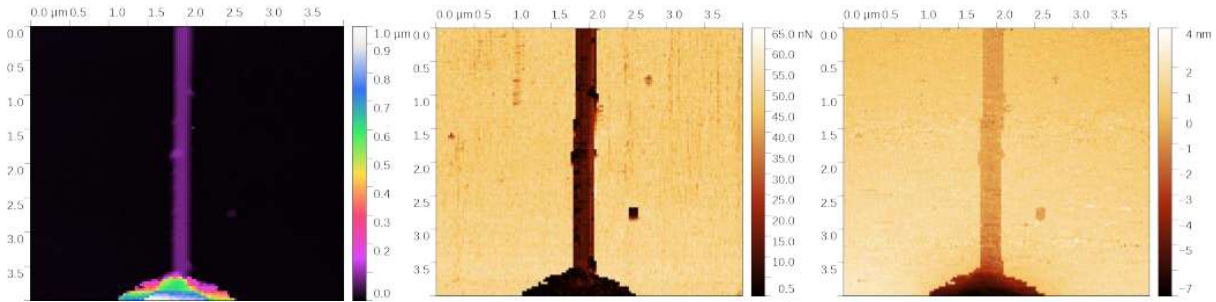
Figure 27. Force Volume operation on a nanowire (topography, adhesion, SThM signal from fixed probe). In the bottom part of the images, we see the fixed probe (i.e. the moving probe scans part of it).

4.2. RESULTS AND INTERPRETATION

Fig. 28 shows the concept of data evaluation and interpretation. Fixed probe was used as a heat source, moving probe was used as heat sink. To interpret the data, we used Finite Difference Method [10], searching for the nanowire thermal conductivity that would fit best the experimental data. As the absolute values of all the signals are subject to drifts and offsets, we concentrated on using the non-linear dependence of signals across the scan. By fitting the shape of SThM signal profiles across the surface we can get rid of the absolute values. This also makes a comparison to a numerical model much easier, as it is hard to convert the SThM voltage to a heat power.
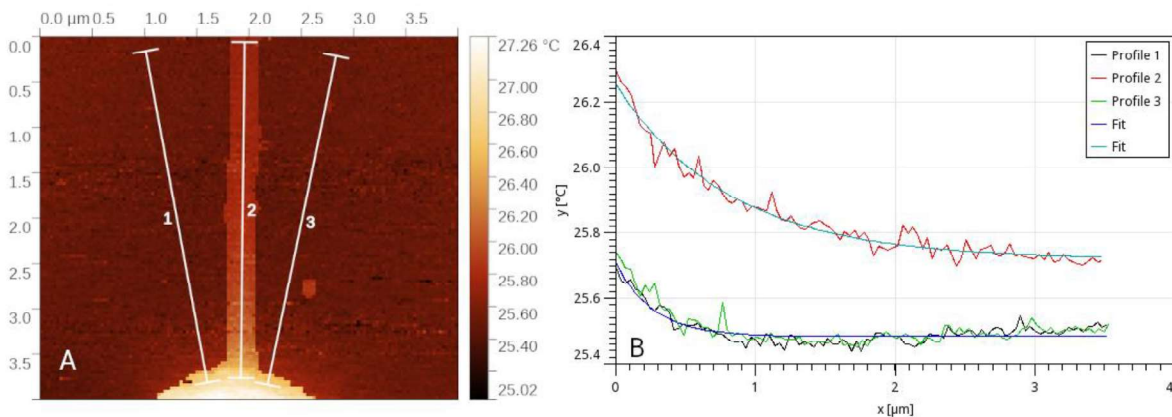

Figure 28. Fitting based evaluation of the nanowire conductivity: profiles across the nanowire and across the substrate and their exponential fits.

Fig. 29 shows the numerical model and result of the analysis. The numerical model has many weaknesses, namely using only diffusive heat transport, so it can be used only to get very approximate thermal conductivity values. Nevertheless, it was used here to demonstrate that the two-probe method is enough sensitive to generate data that can be evaluated quantitatively.

Uncertainty of the measurements using the two-probe setup can be split into the positioning related and thermal measurements related part. From the point of positioning, i.e. probe-probe distance, the benefit of the setup is that the standard SPM accuracy (typically 0.5% on a commercial instrument) can be expected in the case when we image the fixed probe during the measurement. In this case the biggest positioning uncertainty in lateral direction is related to fixed probe mechanical drift, which was measured to be up to 100 nm/hour. In the z direction the uncertainties remain comparable to a standard SPM as the probes are in the contact with the surface. From the point of thermal measurements, the standard uncertainties for a single SThM apply to both probes (discussed e.g., in Good Practice Guide No. 2 developed in this project). When the fixed probe is used without feedback, the contact resistance related uncertainty however needs

EMPIR   EURAMET

The EMPIR initiative is co-funded by the European Union's Horizon 2020
research and innovation programme and the EMPIR Participating States

to be increased. As discussed above, the biggest uncertainty when coming to data interpretation – from conductance between the two probes to thermal conductivity of a particular object, is related to the choice of numerical model.
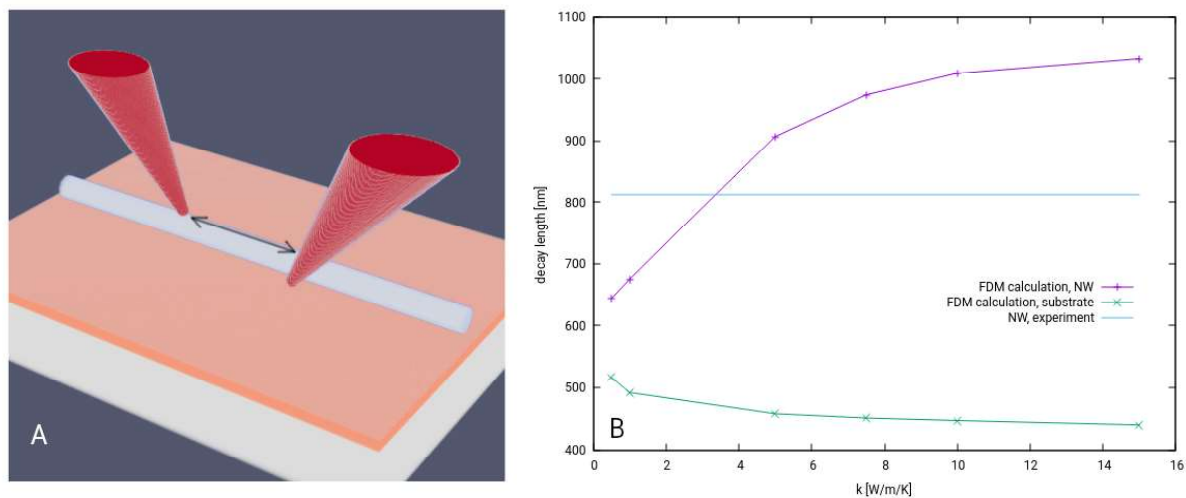
Figure 29. Use of numerical model (A) to preliminary estimate the NW thermal conductivity from the exponential fits shown in Fig. 28B.

5. CONCLUSIONS

We have reported two methodologies that enable thermal transport measurements on individual nanowires. The NWs tested are produced by MACE and consist of ZnO-coated porous Si NWs. The first technique uses microfabricated suspended structures to minimize thermal losses. It provides accurate measurements of thermal conductance with uncertainties around 10% at the expense of a lengthy and complex preparation protocol to hang the NW onto the suspended nitride beams. The second methodology is much faster, since the NW lie directly on a substrate, though absolute accuracy is more difficult to achieve.

References

1. M. Muñoz-Rojo et al. *Review on measurement techniques of transport properties of nanowires,* Nanoscale **5**, 11526 (2013).
2. E. Cara, L. Mandrile, L. Ferrarese et al. *Influence of the long-range ordering of gold-coated Si nanowires on SERS*. Sci. Rep 8, 11305 (2018).
3. Z. Huang, N. Geyer, P. Werner, J. De Boor, U. Gösele, *Metal-assisted chemical etching of silicon: A review*. Advanced Materials vol. 23 285–308 (2011).
4. Kim et al., *A four-probe thermal transport measurement method for nanostructures*, Rev. Sci. Instrum. **86**, 044901 (2015).
5. M. Noyong, K. Blech, A. Rosenberger, V. Klocke and U. Simon, *In situ nanomanipulation system for electrical measurements in SEM*, 2007 Meas. Sci. Technol. 18 N84 DOI 10.1088/0957-0233/18/12/N02.
6. Ferrando-Villalba et al. *Impact of pore anisotropy on the thermal conductivity of porous Si nanowires* Scientific Reports, **8**(1), 12795 (2018).
7. Ferrando-Villalba et al., *In-plane thermal conductivity of sub-20 nm thick suspended mono-crystalline Si layers,* Nanotechnology, **25** (2014) 185402.

8. LA. Giannuzzi, JL. Drown, SR. Brown, RB. Irwin, FA. Stevie, *Applications of the FIB lift-out technique for TEM specimen preparation*. Microscopy Res Tech. **41**, 285-290, (1998).

9. Y. Kim, J. Seo, JY. Lee, J. Ahn, *Advanced Methodologies for Manipulating Nanoscale Features in Focused Ion Beam*. Adv. Mat. **45**, 208-213, (2015). https://doi.org/10.9729/AM.2015.45.4.208.

10. P. Klapetek, J. Martinek, P. Grolich, M. Valtr, N. J. Kaur, *Graphics cards-based topography artefacts simulations in Scanning Thermal Microscopy*, International Journal of Heat and Mass Transfer, **108** (2017) 841–850.